THE JOURNAL OF PHYSICAL CHEMISTRY C

Article

Cite This: J. Phys. Chem. C 2017, 121, 25632-25640

pubs.acs.org/JPCC

Synthesis of Carbon Nanotubes Networks Grown on Silicon Nanoparticles as Li-Ion Anodes

Gal Grinbom,[†] Merav Muallem,[†] Anat Itzhak, David Zitoun,* and Gilbert D. Nessim*

Department of Chemistry and the Bar-Ilan Institute for Nanotechnology and Advanced Materials, Bar-Ilan University, Ramat Gan, 52900, Israel

Supporting Information

ABSTRACT: Using chemical vapor deposition, we grew carbon nanotubes (CNTs) on the surface of Si nanoparticles (NPs) that were coated with a thin iron shell. We studied the CNT growth mechanisms and analyzed the influence of (1) varying annealing times and (2) varying growth times. We show that an initial annealing is necessary to reduce the iron oxide shell and to start the formation of Fe NPs and their consequent coarsening. We characterize the evolution of the catalyst morphology and its influence of the morphology and structure of the CNTs grown. We studied this nanocomposite of Si NPs interconnected by CNTs grown on them as anode material for Li-ion batteries. Compared to the pristine Si NPs, the Si-CNT nanocomposite brings an increase of 40% in specific capacity after 100 cycles at 1800 mA/g_{Si} with a high stability and a very low capacity loss per cycle of 0.06%. The electrochemical performance demonstrates how efficient the CNT shell on the Si NP is to mitigate the usual failure mechanism of Si NPs. Thus, the in situ growth of CNTs on Si anode materials can be an efficient route toward the synthesis of more stable Si anode composites for a Li-ion battery.

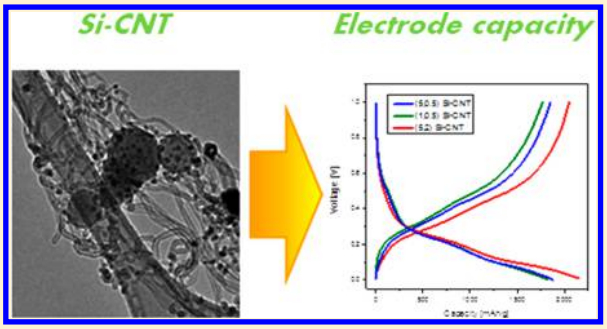

1. INTRODUCTION

The combination between Si nanoparticles (NPs) and carbon nanotubes (CNTs) has attracted great interest in recent years due to their promise for future applications in Li-ion batteries. Silicon has the highest theoretical gravimetric capacity of 3600 mAh g^{-1} among all possible anode materials;[1−3] therefore, it is an attractive candidate for advanced high energy Li-ion batteries. However, Si cracks due to mechanical stresses upon cycling because of its high volume expansion during lithiation, with consequent loss of electrical contact. To improve the cyclability of Si-based anodes, the mixing of Si NPs with CNTs was studied in recent years. CNTs are known for their good electrical conductivity, high mechanical strength and structural flexibility, and their ability to form an efficient conductive network.[4−8] A tangled CNT network in the electrode can help to prevent cracking and pulverization, to maintain the integrity of electrodes, and to stabilize the electronic conductive network, eventually leading to better cycling performance.[1,9−13]

Several techniques for Si NP and CNT integration were proposed, such as simple mechanical mixing with small Si NPs (average diameter of 10 nm), resulting in decorating the Si NPs on the surface of CNTs,[14−18] or with larger Si NPs (30−100 nm in diameter) that were dispersed in a CNT network.[19−22] Others proposed Si NP-filled CNT structures,[23] covalent bonding between Si NPs and CNTs,[12,24] growth of CNTs on Si,[25,26] core−shell of CNTs and silicon-based precursor-derived glass-ceramics (no binder with spray).[27]

The presence of CNTs close to Si NPs by covalent bonds, as shown by Martin et al.,[12] enhanced the electronic pathway to the active material particles and helped to prevent silicon destruction upon repeated lithium insertion/extraction by improving the mechanical stability of the electrode at the nanoscale level. This effect resulted in increased cycling ability and higher capacity in the composite electrode compared to the simple mixture of the two compounds.[24] This phenomenon has been shown also with graphene oxide chemically contacted to Si.[28]

When CNTs were directly grown on the surface of Si NPs, the composite showed a reversible capacity of ∼1500 mAh g^{-1} after 20 cycles.[25] This high capacity can be attributed to the maintenance of a good electronic conducting network due to the robust adherence of the CNTs to the Si NPs and to the flexibility of the nanotubes that can accommodate the volume change of Si upon lithium alloying and dealloying.

Here, we pushed further into the study of the direct growth of CNTs on Si NPs to improve the anode material in Li-ion batteries. Using chemical vapor deposition (CVD), we controlled the morphology of the CNTs grown on the surface of Si NPs.

We will show the morphology evolution of the catalytic iron shell (on the Si NPs) during annealing and CNT growth, where

Received: June 11, 2017
Revised: September 26, 2017
Published: November 1, 2017

DOI: 10.1021/acs.jpcc.7b05709
J. Phys. Chem. C 2017, 121, 25632−25640

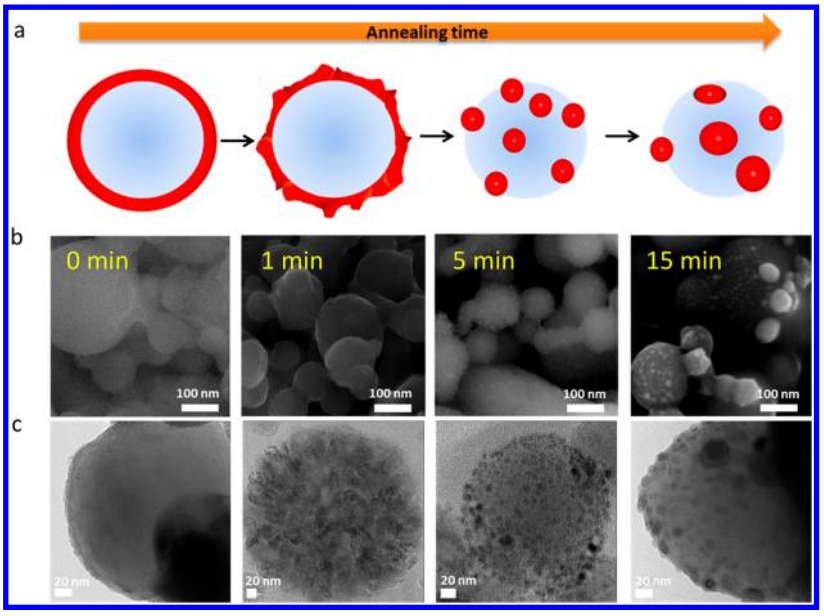

Figure 1. Scheme (a), HR-SEM images (b), and TEM images (c) showing the evolution of the iron nanoparticles on the Si surface for different annealing times. From a shell on the Si particles before annealing (0 min), via homogeneous small nanoparticles (1−5 min, 6−9 nm diameter size), to larger and nonuniform iron particles after 15 min of annealing. In the pictorial above, the red represents the iron and the blue represents the silicon.

the thin layer converts to small particles which subsequently coarsen, similar to the morphology evolution of iron on a Si wafer.[29] We will also show how annealing time and growth time affect the morphology and structure of the CNTs grown.

Moreover, we characterized the electrochemical properties of the Si-CNT nanocomposites, by performing cyclic voltammetry (CV) and galvanostatic measurements. While the CV results are comparable for Si NPs with and without the CNT grown on top, the galvanostatic measurements demonstrate the higher stability of the Si-CNT nanocomposite.

2. EXPERIMENTAL SECTION

2.1. Si-Fe Nanoparticles Preparation. To produce Si NPs with an iron-oxide shell, we mixed two solutions: (1) 0.082 g of Si NPs with an average diameter of 100 nm (Sigma-Aldrish) dispersed in 3 mL of 1-octadecene, and (2) 0.1 mL of $Fe(CO)_5$ solubilized in 2 mL of 1-octadecene. We stirred the mixture at 300 °C for 3 h. Then, in order to separate the solid from the dispersion, we centrifuged the solution for 100 min at 6000 rpm, and redispersed the dark brown solid in dry ethanol. We repeated the last two steps three times and dried the dispersion under vacuum overnight to evaporate the ethanol.

2.2. Si-Fe-CNT Preparation. To synthesize CNTs on the Si-Fe NPs, we used a thermal chemical vapor CVD system consisting of a three-zone furnace and a fused silica (quartz) tube with a 25 mm external diameter and 22 mm internal diameter. The first two zones preheated the precursor gases to decompose the hydrocarbons and to form controlled ppm's of water vapor from oxygen and hydrogen.[30,31] The positive role of water vapor in extending catalyst lifetime was first shown in 2004 by Hata et al.,[32] where, by adding ppm's of water vapor during CNT growth, they first grew millimeter-tall CNT forests of vertically aligned CNTs. In our synthesis, we form the ppm's of water vapor in situ by preheating oxygen (1% oxygen contained in an Ar tank) with hydrogen to form water vapor.[31]

The sample was introduced on an alumina boat into the third zone of the furnace using the fast heat technique to start the thermal process with annealing gases and temperatures at equilibrium.[33] The gases used were Ar (99.9999%), Ar/O_2 (a mixture with 99% Ar and 1% O_2), C_2H_4 (99.999%), and H_2 (99.9999%). Gas flows were controlled by electronic mass flow controllers (MKS P4B) with a digital mass flows control unit (MKS model 247D). The two preheating zones were set at 770 °C and the growth zone was set at 650 °C.

The steps in the process were (1) purge with Ar and H_2 (100 and 400 sccm) for 15 min at room temperature with the sample positioned outside the furnace; (2) introduce the sample into the growth zone and anneal for varying durations (0−15 min) under the same Ar/H_2 gas flows; (3) introduce C_2H_4 (200 sccm) and Ar/O_2 (100 sccm) to grow CNTs for varying durations (0−5 min); (4) turn off the Ar/O_2 and C_2H_4, with Ar and H_2 post-anneal 1 min; and (5) turn off H_2 and finally push the tube outside the furnace to cool under only Ar flow prior to sample removal.

2.3. Characterization. We characterized the samples using high-resolution scanning electron microscopy (HRSEM, Zeiss 982), transmission electron microscopy (TEM, JEM-1400, JEOL), Raman spectroscopy (Renishaw Raman spectrometer) with a laser frequency of 514 nm, and CHNS elemental analysers (FlashEA 1112, Thermo). We measured the capacity by CV measurements (biologic).

All work was conducted in an argon-filled glovebox. Electrode materials (Si and Si-CNT) were laminated onto a roughened copper foil (Oxygenfree, SE-Cu58, Schlenk Metallfolien GmbH & Co. KG). The silicon powder was uniformly spread on the surface, and adhesion to the current collector was enhanced by applying manual pressure with Kimwipe papers. The loading was measured by ICP-AES analysis and by weight using an analytical balance. On average, the loading was roughly 0.1 mg/cm^2 of silicon.

The anodes were tested in coin-type cells (2523, NRC, Canada) vs lithium metal (Chemetall Foote Corporation, USA). The electrolyte solution was fluoroethylene carbonate FEC (Aldrich, < 20 ppm water) and dimethyl carbonate DMC

DOI: 10.1021/acs.jpcc.7b05709
J. Phys. Chem. C 2017, 121, 25632−25640

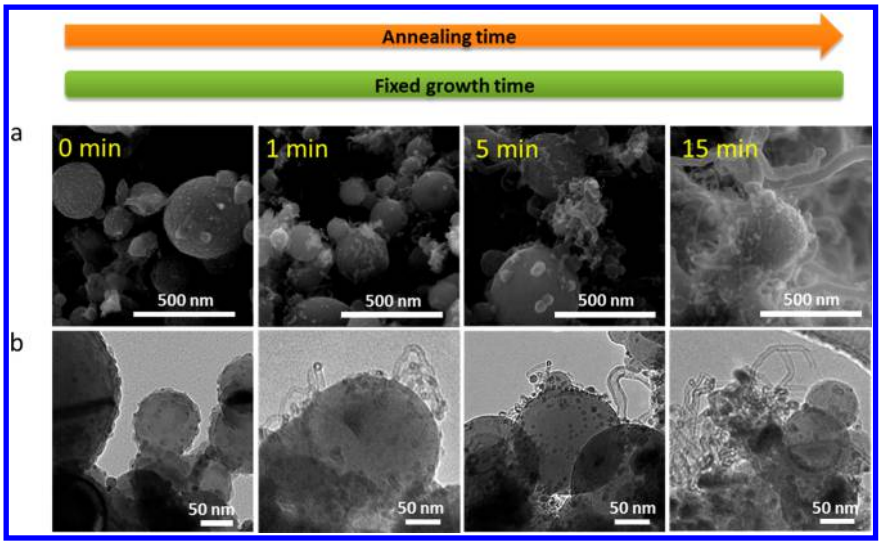

Figure 2. HR-SEM (a) and TEM (b) images of the samples with different annealing times, 0−15 min, and fixed CNT growth time of 30 s.

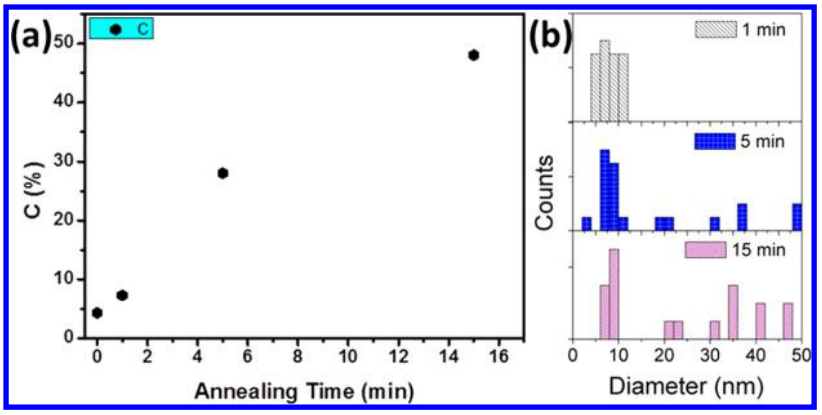

Figure 3. (a) Carbon content evolution from elemental analysis of the sample as a function of the annealing time of Si-Fe NPs. (b) Histogram of the distribution of CNT diameters as a function of the annealing time (measured from HRTEM images).

(Aldrich, < 20 ppm water) (1:4 ratio) with 1 M LiPF6 (Aldrich). The cells were assembled in an argon-filled glovebox, with a purifying system (MBraun GmbH, Germany), oxygen and water contents below 1 ppm.

Cyclic voltammetry was measured with a Bio-Logic VMP3, multichannel potentiostat at 0.1 mV/s between 1 and 0 V vs Li^+/Li to obtain relevant electrochemical processes characterization. Coin cells were cycled at 30 °C using a BT2000 battery cycler (Arbin Instruments, USA) (first three discharge: C/10, therefore, C rate: all capacity in 1 h).

3. RESULTS AND DISCUSSION

Most of the Si NPs used in this research exhibit a round shape, although we also found some with an oval shape, with sizes ranging from 50 to 100 nm in diameter. Following a procedure discussed in our previous publication,[34] we coated the nanoparticles with an iron oxide Fe_2O_3 shell through an organometallic pathway, resulting in Si-Fe_2O_3 NPs. In order to study the growth of CNTs on the Si-Fe_2O_3 NPs and to be able to control it, we chose to anneal the nanoparticles at temperatures below 650 °C under a flow of Ar/H_2. Had we grown CNTs at the usual temperatures above 700 °C, the growth kinetics would have been too fast to properly characterize the CNT growth process.

As we will describe below, we observed CNTs with different diameters, which depended on the synthesis parameters (annealing and growth times). However, since the CNTs grown are entangled, we could not measure their length accurately, but could only estimate it.

In order to study the effect of the annealing duration on the morphology of the iron shell, i.e., on the Si surface, we annealed the samples under a flow of argon and hydrogen at 650 °C for different times, ranging from 0 to 15 min. We then characterized the samples using HR-SEM (Figure 1). We found that the iron shell, approximately 5 nm thick in the form of Fe_2O_3, was reduced and started to form Fe clusters in the first minute of the annealing process under an Ar/H_2 flow. Next, we observed the formation of homogeneous small nanoparticles, 6−9 nm diameter size on the Si NP surface. When we increased the annealing time to 15 min, the iron nanoparticles coarsened, resulting in larger Fe particles on the Si NPs with diameters ranging from 10 to 50 nm.

To study the CNT growth on the Si-Fe_2O_3 NPs, we first annealed the NPs under argon and hydrogen flow at 650 °C for different times, ranging from 0 to 15 min, as mentioned above. Immediately after the annealing step, we introduced the carbon source, ethylene, and Ar/O_2 (Ar with 1% O_2) in the reactor for 30 s. The HRSEM and TEM images of these samples are shown in Figure 2. We observed CNT growth on the Si-Fe NPs

DOI: 10.1021/acs.jpcc.7b05709
J. Phys. Chem. C 2017, 121, 25632−25640

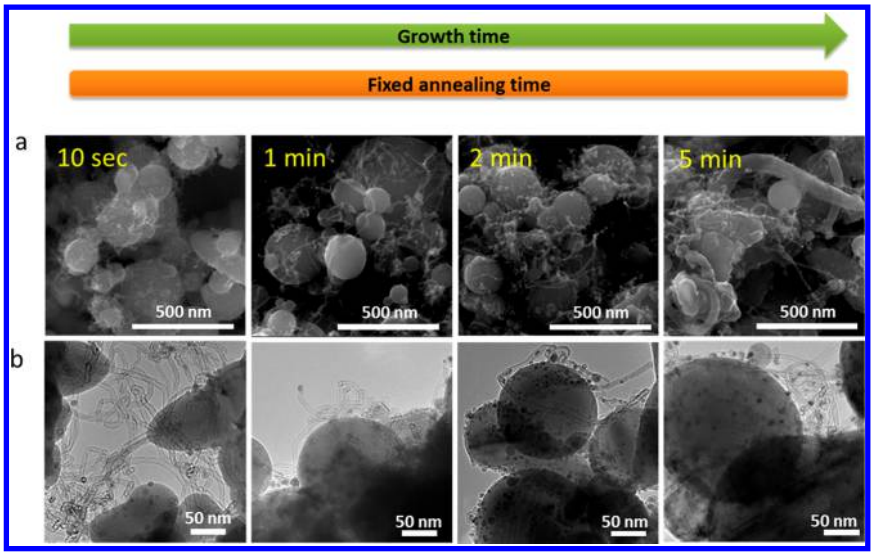

Figure 4. HR-SEM (a) and TEM (b) images of the samples with 5 min annealing, and different growth times, from 10 s to 5 min.

only in the samples that were annealed for 1 min or more, while no CNT growth was present for the samples without the annealing step. This indicates that a reducing annealing step is necessary to reduce the Fe_2O_3 shell to then form the metallic iron catalyst nanoparticles.[35] However, CHNS analysis (Figure 3) showed an amount of 4.3% of carbon in the nonannealed sample, possibly organic residues on the iron oxide shell.

When the Si-Fe NPs were first annealed, Fe NPs formed and CNTs grew on them. For increasing annealing durations, we observed a higher distribution of the iron NPs on the Si surface (as shown before for only the annealing step, Figure 1). For a short annealing time (1 min), we observed CNTs with an average diameter of 8.7 nm. However, for an annealing time of 5 min, the CNT diameters ranged from 6 to 50 nm. We observed similar results for the 15 min annealed samples.

In parallel to the increase in CNT diameter, the percent of carbon atoms also increased with annealing time. As previously mentioned, in the sample that was not annealed before the growth step, we found 4.3% of carbon. When we increased the annealing time to 1 min, the amount of carbon increased to 7.3%, an increase of 1.7×. For 5 min annealing, we measured 28% of carbon (7 times higher) and reached 48% of carbon for 15 min (11 times more carbon compared to no annealing). We can attribute this jump in the amount of carbon atoms diffusing into the larger, coarsened iron particles that formed during the annealing step, thus growing larger diameter CNTs.

We then fixed the annealing time (5 min), varied the duration of the growth step from 10 s to 5 min, and characterized the CNTs grown on the Si-Fe NPs. The HR-SEM and TEM images of these samples are shown in Figure 4. For only 10 s growth, we observed uniform CNT covering of the NPs. The CNTs are thin, with an average diameter of 6.5 nm. We observed similar results for 1 min growth. In addition, from the chemical elemental analysis (Figure 5), we noticed that the carbon content of the two samples was also similar, with 31.7% and 33.4% for the 10 s and 1 min samples, respectively. However, we observed a jump in the carbon content after 2 min of growth (44% carbon content), where we observed a nonuniform distribution of CNT diameters (from 6 to 64 nm). A 5 min growth process led to a 50% carbon content with the growth of carbon nanofibers (CNFs) with diameters around 100 nm next to thin CNTs (diameters below 10 nm).

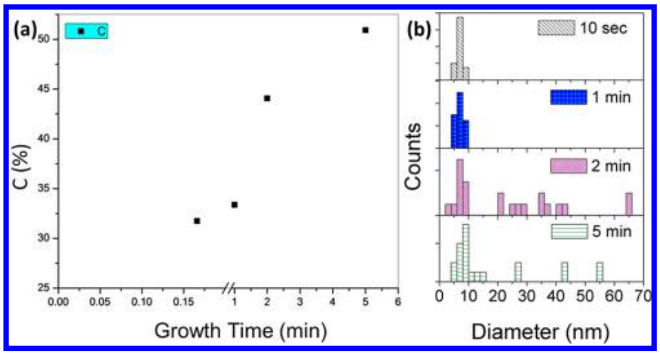

Figure 5. (a) Carbon content evolution from elemental analysis of the sample as a function of the growth time. (b) Histogram of the distribution of CNT diameters as a function of the growth time (from HRTEM measurements).

When we analyzed the carbon content for different annealing, or growth durations, we noticed how critical the annealing step was for CNT growth. For instance, the sample annealed for 5 min with a short 10 s growth showed 7 times more carbon content compared to the sample without annealing, but with a 30 s growth duration (3 times longer growth duration). HRTEM images of the CNTs grown on top of the Si NPs clearly show the walls of the CNTs, indicating that the CNTs grown are multiwalled and with good graphitization (Figure 6). Raman analysis confirmed this by exhibiting the three main peaks at a Raman shift of 2700 cm^{-1} (2D or G′ band), 1581 cm^{-1} (G band), and 1338 cm^{-1} (d band), which are in agreement with MWCNT spectra. Furthermore, when focusing on the G band peak, we observed a broadening of the peak, mainly around 1605 cm^{-1} (D′ band)—this broadening suggests a D′ peak, which is typical of MWCNTs (Figure S1).[36,37]

We named the samples according to the annealing time and the growth time. For example, "(5,2) Si-CNT" corresponds to 5 min annealing time and 2 min of growth time. The thickness of the CNTs in these samples was measured using the HRTEM images, and the diameter distribution histograms of Si-CNT samples are shown in Figure 3 (anneal) and Figure 5 (growth). We assembled Li-ion batteries with all the composite materials as binder-free anodes directly on the spacer. The absence of

DOI: 10.1021/acs.jpcc.7b05709
J. Phys. Chem. C 2017, 121, 25632−25640

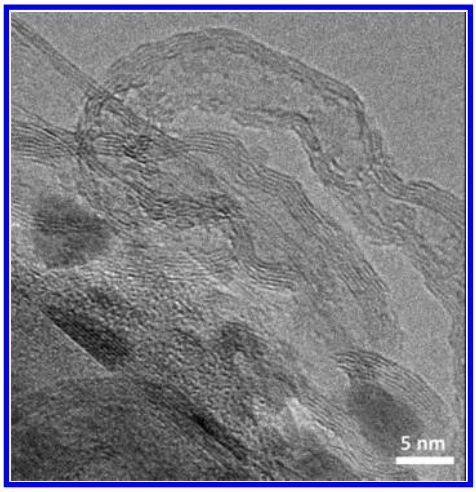

Figure 6. HRTEM image of CNTs, grown for 2 min and annealed for 30 s, shows MWCNTs with few walls.

binder allows us to evaluate the electrochemical properties of the active material alone. All the composite materials have been tested, and we report below the in-depth study of the best material (5,2) Si-CNT (Figures 7 and 8), followed by the galvanostatic cycling of the other composite materials.

In order to study the electrochemical properties of this composite nanostructure, we tested the (5,2) Si-CNT as binder-free electrodes in the coin cells versus a Li metal counter electrode in an electrolyte solution of 1 mol/L $LiPF_6$ in fluoroethylene carbonate/dimethyl carbonate (FEC/DMC) 1:4 ratio. The first assessment is obtained through the CV of the electrodes, which gives the fingerprints of the silicon alloying and dealloying process with Li.

Figure 7a shows the CV measurement of the pristine Si NPs and (5,2) Si-CNT samples grown with 5 min annealing and 2 min growth. The black curves represent the pristine Si sample, and the red curves represent the (5,2) Si-CNT sample. The first cycles are shown in dashed lines, and the continuous lines are the 4th cycle. The electrodes of the pristine Si and (5,2) Si-CNT display a typical CV for silicon. We observe two lithiation plateaus at 0.2 and 0.06 V vs Li in discharge and delithiation at 0.3 and 0.45 V vs Li in charge. These two events correspond to the formation of two main phases of Li_xSi_y alloys.[2,3,38] The first CV of the (5,2) Si-CNT shows a reduction peak at 1.4 V which is not present in the pure Si electrode. The reduction peak observed during the first lithiation is irreversible in the potential window [0−1 V]. As shown in a previous study, the Li insertion at 1.4 V is consistent with the conversion reaction of Fe_2O_3.[34] The low potential lithiation close to 0 V is attributed to the alloying of crystalline silicon with lithium to yield amorphous lithiated silicon.[3]

In a controlled experiment, we tested the Si NPs coated with Fe with the same thickness of Fe coating used for catalyst growth (Figure 7b). The Si-Fe were submitted to the same thermal treatment as for the CNT growth, but without a carbon source (C_2H_4). The cyclic voltammetry is typical of Si while the first lithiation shows the irreversible conversion reaction of iron oxide. As reported previously,[31] the Si-Fe core/shell particles do not display an enhancement in terms of specific capacity.

Figure 8a shows the specific capacities measured for Si and (5,2) Si-CNT electrodes for over 300 cycles. All capacities are normalized to the mass of Si. The stability in cycling and the Coulombic efficiency are shown in Figure 8a for a single cell

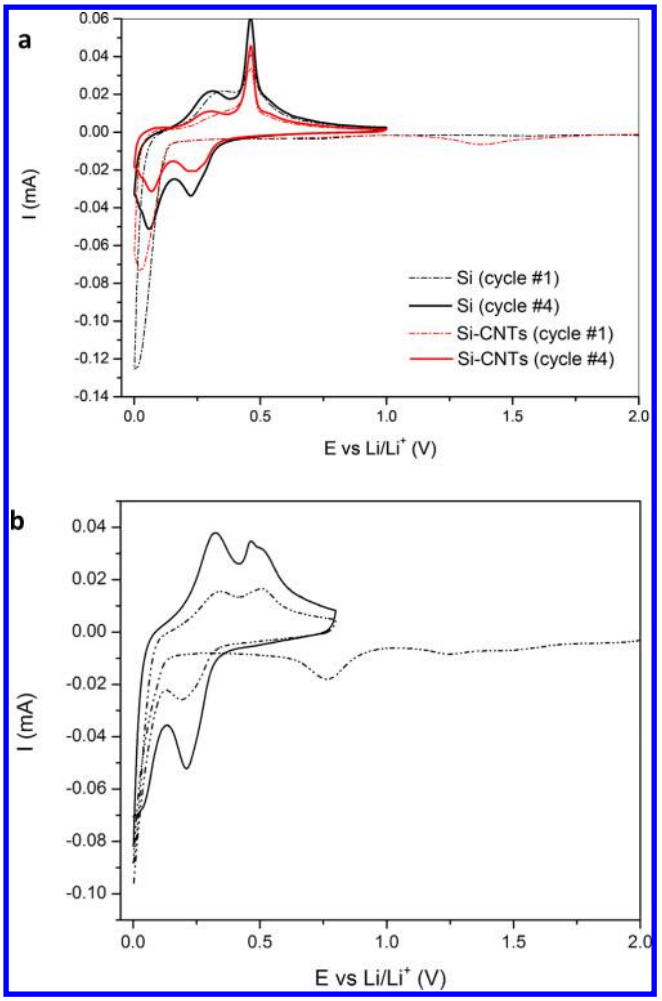

Figure 7. Cyclic voltammetry of Si NP and (5,2) Si-CNT during the 1st cycle and 4th cycle (a). Cyclic voltammetry of Si-Fe NPs without CNT growth (cycle #1 dashed line; cycle #4 plain line) (b).

and Figure 8b on several cells over 70 cycles. The specific capacity of Si NPs after 100 cycles is 1300 mAh/g_{Si}, and the capacity of (5,2) Si-CNT NPs reaches 1800 mAh/gSi, an almost 40% increase in a specific capacity. The stability in the cycling of the (5,2) Si-CNT is higher than the stability of pristine Si NPs, as can be seen from the very low capacity loss per cycle achieved with the composite. The (5,2) Si-CNT composite displays a capacity loss of only 0.06%/cycle compared to 0.2%/cycle for the pristine Si. After the first discharge irreversible capacity loss, the reversible capacity loss is extremely low for a Si anode. The Coulombic efficiency also demonstrates the higher efficiency of the (5,2) Si-CNT vs the pristine Si.

All the Si-CNT electrodes demonstrate a high capacity above 1500 mA/g_{Si} for the 50th cycle and very good stability. In order to understand whether the thickness and amount of CNTs need to be considered while optimizing the electrode, we compared samples prepared with different annealing and growth times. Figure 9 summarizes the results of galvanostatic cycling for the samples (5,2) Si-CNT, (5,0.5) Si-CNT (5 min annealing and 30 s growth), and (1,0.5) Si-CNT (1 min annealing and 30 s growth). As the annealing time increases from 1 to 5 min, the capacity for the 20th cycle slightly increases from 1820 to 1880 mAh/g. The annealing time has a very little effect on the electrochemical properties.

DOI: 10.1021/acs.jpcc.7b05709
J. Phys. Chem. C 2017, 121, 25632−25640

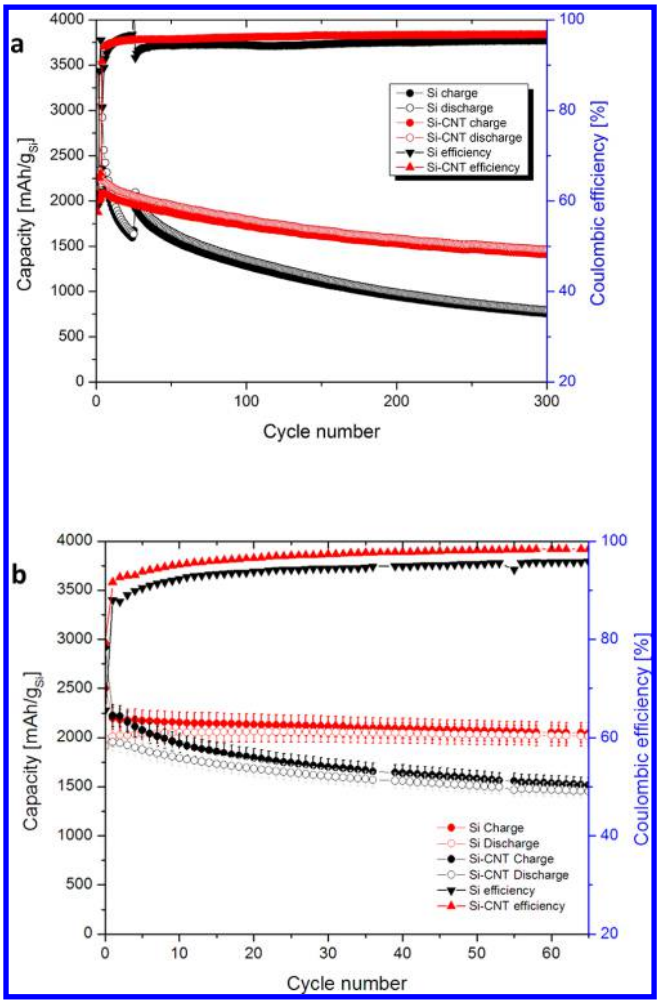

Figure 8. Galvanostatic cycling over 300 cycles at C rate of a typical Li-ion half-cell with Si NP as anode material (black dots) and (5,2) Si-CNT (red dots) with their respective Coulombic efficiency (black and red triangles, respectively) (a). Average values of Li-ion half-cell over 70 cycles at C rate with Si NP as anode material (black dots) and (5,2) Si-CNT (red dots) with their respective Coulombic efficiency (black and red triangles, respectively); the error bars show the standard deviation from the four batteries (b).

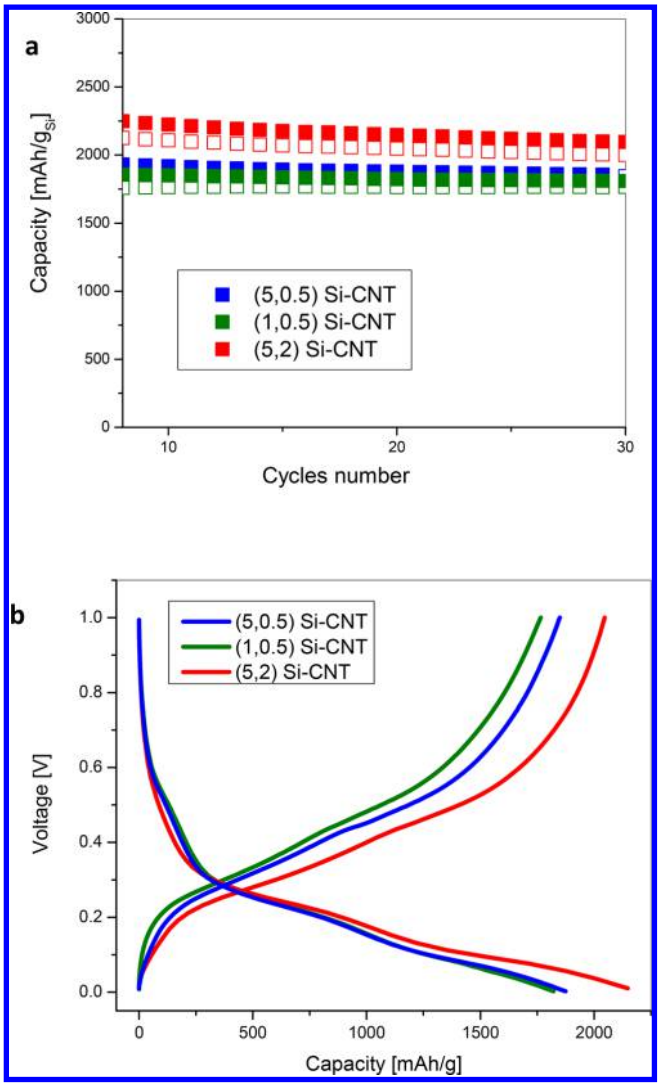

Figure 9. Galvanostatic charge and discharge capacity at C rate of (5,2) Si-CNT (red), (1,0.5) Si-CNT (green), and (5,0.5) Si-CNT (blue) (charge: full square; discharge: empty squares) (a). Corresponding voltage profiles for the 20th cycle of Si-CNT samples (b).

On the other hand, (5,0.5) Si-CNT and (5,2) Si-CNT exhibit the same annealing time with different growth times. The 2 min growth sample displays a significantly higher capacity of 2150 mAh/g (compared to 1880 mAh/g). Figure 9b shows the voltage profile of charge and discharge. Interestingly, the (5,0.5) Si-CNT and (5,2) Si-CNT samples have different amounts of CNTs (35% vs 44% in weight). The CNTs themselves have a similar thickness (Figure 3b). Therefore, we can conclude that the capacity is increased with increasing number of CNT connections between the Si particles.

The electrochemical results reported above are independent of any formulation requirement or structuration of the electrode. The "binder-free" approach allows attributing the rise in the performance of the electrode to the sole Si-CNT active materials. These results confirm the good stability of the 3D porous silicon-MWNT heterostructures previously achieved.[26] The reported capacity fading of 0.07% reported is slightly higher than the capacity fading of 0.06% of the Si-CNT composite in the present study. Overall, both studies show how promising the Si-CNT composite can be when the growth process is timely engineered.

The CNTs grown directly on the Si electroactive material are playing a major role on the excellent electrochemical properties observed for the batteries. The electrodes before cycling show the CNTs interconnecting the Si particles (Figure 10A,C and Figure S2). This connection allows for the volume expansion of Si upon cycling while maintaining the electrical connections, like a flexible net wrapping each particle. Upon cycling, this morphology is maintained, as evidenced by the post-mortem HR-SEM images of the electrodes (Figure 10B,D), with the CNTs still wrapping the Si particles in the flexible net. These geometrical constraints explain the high capacities and Coulombic efficiencies reported for the Si-CNT compared to the analogous Si NPs.

The chemical composition of the electrodes after cycling has been collected after cycling the Si NPs and the Si-CNTs (Figure 11). The SEM has been operated at four different voltages to provide different penetration depths and to give a qualitative profile of the chemical compositions. The estimated

DOI: 10.1021/acs.jpcc.7b05709
J. Phys. Chem. C 2017, 121, 25632−25640

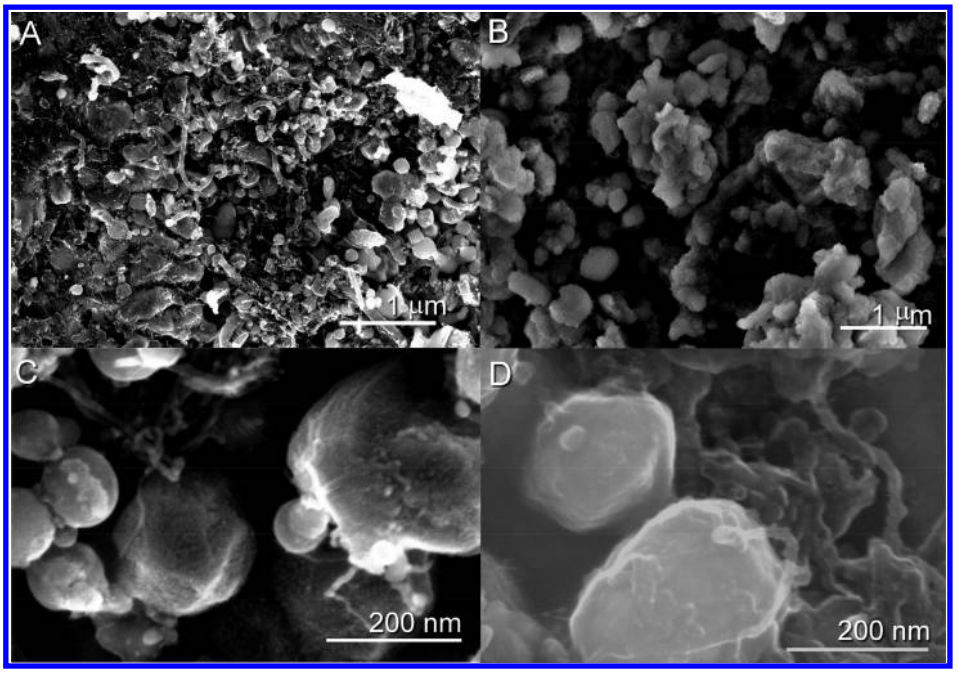

Figure 10. HR-SEM images of the Si-CNT electrodes before cycling (A, C) and after cycling at C rate (B, D).

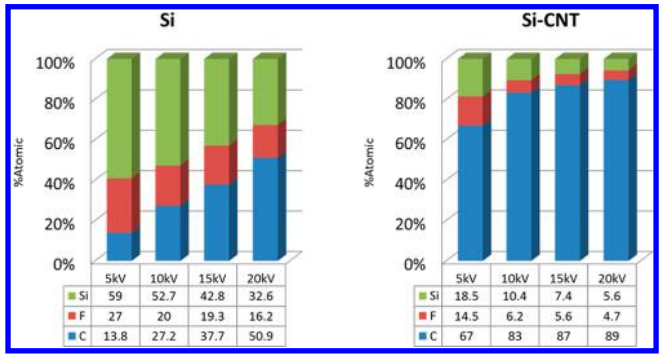

Figure 11. EDS of the Si and Si-CNT electrodes after cycling at C rate at different acceleration voltages.

depth can be calculated through the Anderson and Hasler's model as $Z_D = 64\frac{E_0^{1.68}}{\rho}$, where E_0 is the energy (keV) and ρ is the layer density.

A large amount of fluor is found on the upper layer of the Si electrode (27%) and Si-CNT electrode (18.5%). The high F content demonstrates the formation of byproducts by decomposition of FEC and $LiPF_6$ during the cycling. The amount of F decreases while the amount of C increases, suggesting that the lower F content in the Si-CNT corresponds to the formation of a solid electrolyte interphase (SEI) on the CNTs and less on the Si. The formation of an SEI on carbonaceous materials is well-known and understood. The Si-CNT composites grow an SEI partially on the Si and mainly on the CNT shell surrounding the Si particles as shown in Figure 10B.

4. CONCLUSIONS

We studied the synthesis of CNTs directly grown on top of Si NPs. The annealing of Si-Fe_2O_3 at the beginning of the process is important since hydrogen reduces the Fe_2O_3 shell to form metallic Fe catalyst particles on the Si surface, which become the catalysts for CNT growth. The annealing time of the Si-Fe controls the iron NP size and therefore the diameter of the CNTs. We found that the ideal annealing time for thin and uniform CNTs is 2 min. As expected, the growth time modulates the length of the CNTs. For growth times above 5 min (after 5 min of annealing), carbon nanofibers (CNFs) also started to grow. The binder-free electrodes of Si-CNT display the typical alloying−dealloying electrochemical features of nano-Si. Compared to the pristine Si NPs, the Si-CNT nanocomposite brings an increase of 40% in specific capacity after 100 cycles at 1800 mA/g_{Si} with a high stability and very low capacity loss per cycle of 0.06%. The electrochemical performance demonstrates how efficient the CNT shell on the Si NPs is to mitigate the usual failure mechanism of Si NPs. Thus, the in situ growth of CNTs on Si anode materials can be an efficient route toward the synthesis of more stable Si anode composites for a Li-ion battery.

■ ASSOCIATED CONTENT

Supporting Information

The Supporting Information is available free of charge on the ACS Publications website at DOI: 10.1021/acs.jpcc.7b05709.

Raman spectra and TEM images of the Si-CNT composites (PDF)

■ AUTHOR INFORMATION

Corresponding Authors

*E-mail: David.zitoun@biu.ac.il. Tel: +972-3-7384512 (D.Z.).
*E-mail: gdnessim@biu.ac.il. Tel: +972-3-738-4540 (G.D.N.).

ORCID

David Zitoun: 0000-0003-3383-6165
Gilbert D. Nessim: 0000-0003-0738-5436

Author Contributions

†These authors contributed equally.

Notes

The authors declare no competing financial interest.

DOI: 10.1021/acs.jpcc.7b05709
J. Phys. Chem. C 2017, 121, 25632−25640

■ ACKNOWLEDGMENTS

We are grateful to Yafa Pinchas for her help with the elemental analysis. We also want to thank Prof. Jean-Paul (Moshe) Lellouche for generously allowing us to use the Raman spectrophotometer in his laboratory. A partial support for this work was obtained from the Israeli Council for High Education and the Prime Minister Office of Israel in the framework of the INREP project. G.G. thanks the Israeli Ministry of Science, Technology & Space for its financial support (11733-3).

■ REFERENCES

(1) Boukamp, B. A.; Lesh, G. C.; Huggins, R. A. All-Solid Lithium Electrodes with Mixed-Conductor Matrix. *J. Electrochem. Soc.* **1981**, *128*, 725−729.
(2) Key, B.; Bhattacharyya, R.; Morcrette, M.; Seznéc, V.; Tarascon, J.-M.; Grey, C. P. Real-Time NMR Investigations of Structural Changes in Silicon Electrodes for Lithium-Ion Batteries. *J. Am. Chem. Soc.* **2009**, *131*, 9239−9249.
(3) Obrovac, M. N.; Christensen, L. Structural Changes in Silicon Anodes during Lithium Insertion/Extraction. *Electrochem. Solid-State Lett.* **2004**, *7*, A93−A96.
(4) Yu, M.-F.; Lourie, O.; Dyer, M. J.; Moloni, K.; Kelly, T. F.; Ruoff, R. S. Strength and Breaking Mechanism of Multiwalled Carbon Nanotubes Under Tensile Load. *Science* **2000**, *287*, 637−640.
(5) Allaoui, A.; Bai, S.; Cheng, H. M.; Bai, J. B. Mechanical and Electrical Properties of a MWNT/Epoxy Composite. *Compos. Sci. Technol.* **2002**, *62*, 1993−1998.
(6) Salvetat, J.-P.; Bonard, J.-M.; Thomson, N. H.; Kulik, A. J.; Forró, L.; Benoit, W.; et al. Mechanical Properties of Carbon Nanotubes. *Appl. Phys. A: Mater. Sci. Process.* **1999**, *69*, 255−260.
(7) Gao, J.-F.; Li, Z.-M.; Meng, Q.-j.; Yang, Q. CNTs/ UHMWPE Composites with a Two-Dimensional Conductive Network. *Mater. Lett.* **2008**, *62*, 3530−3532.
(8) Hu, N.; Karube, Y.; Yan, C.; Masuda, Z.; Fukunaga, H. Tunneling Effect in a Polymer/Carbon Nanotube Nanocomposite Strain Sensor. *Acta Mater.* **2008**, *56*, 2929−2936.
(9) Du, J.; Zhao, L.; Zeng, Y.; Zhang, L.; Li, F.; Liu, P.; et al. Comparison of Electrical Properties between Multi-Walled Carbon Nanotube and Graphene Nanosheet/High Density Polyethylene Composites with a Segregated Network Structure. *Carbon* **2011**, *49*, 1094−1100.
(10) Wu, H.; Zheng, G.; Liu, N.; Carney, T. J.; Yang, Y.; Cui, Y. Engineering Empty Space between Si Nanoparticles for Lithium-Ion Battery Anodes. *Nano Lett.* **2012**, *12*, 904−909.
(11) Krause, A.; Dörfler, S.; Piwko, M.; Wisser, F. M.; Jaumann, T.; Ahrens, E.; et al. High Area Capacity Lithium-Sulfur Full-cell Battery with Prelitiathed Silicon Nanowire-Carbon Anodes for Long Cycling Stability. *Sci. Rep.* **2016**, *6*, 27982.
(12) Martin, C.; Crosnier, O.; Retoux, R.; Bélanger, D.; Schleich, D. M.; Brousse, T. Chemical Coupling of Carbon Nanotubes and Silicon Nanoparticles for Improved Negative Electrode Performance in Lithium-Ion Batteries. *Adv. Funct. Mater.* **2011**, *21*, 3524−3530.
(13) Cui, L.-F.; Hu, L.; Choi, J. W.; Cui, Y. Light-Weight Free-Standing Carbon Nanotube-Silicon Films for Anodes of Lithium Ion Batteries. *ACS Nano* **2010**, *4*, 3671−3678.
(14) Pan, X.-W.; Liu, N.; Zheng, D.-X.; Shi, M.-M.; Wu, G.; Wang, M.; Chen, H.-Z. Föster Resonance Energy Transfer in Solution-Processed Si-Nanoparticle/Carbon Nanotube Nanocomposites. *Nanotechnology* **2009**, *20*, 415605.
(15) Zhu, X.; Xia, B.; Guo, M.; Zhang, Q.; Li, J. Synthesis of Carbon Nanotube Composites with Size-Controlled Silicon Nanoparticles. *Carbon* **2010**, *48*, 3296−3299.
(16) Wang, W.; Kumta, P. N. Nanostructured Hybrid Silicon/ Carbon Nanotube Heterostructures: Reversible High-Capacity Lithium-Ion Anodes. *ACS Nano* **2010**, *4*, 2233−2241.
(17) Gohier, A.; Laïk, B.; Kim, K.-H.; Maurice, J.-L.; Pereira-Ramos, J.-P.; Cojocaru, C. S.; et al. High-Rate Capability Silicon Decorated Vertically Aligned Carbon Nanotubes for Li-Ion Batteries. *Adv. Mater.* **2012**, *24*, 2592−2597.
(18) Feng, X.; Ding, T.; Cui, H.; Yan, N.; Wang, F. A Low-Cost Nano/Micro Structured-Silicon-MWCNTs from Nano-Silica for Lithium Storage. *Nano* **2016**, *11*, 1650031.
(19) Bae, J. Fabrication of Carbon Microcapsules Containing Silicon Nanoparticles−Carbon Nanotubes Nanocomposite by Sol−Gel Method for Anode in Lithium Ion Battery. *J. Solid State Chem.* **2011**, *184*, 1749−1755.
(20) Xue, L.; Xu, G.; Li, Y.; Li, S.; Fu, K.; Shi, Q.; et al. Carbon-Coated Si Nanoparticles Dispersed in Carbon Nanotube Networks As Anode Material for Lithium-Ion Batteries. *ACS Appl. Mater. Interfaces* **2013**, *5*, 21−25.
(21) Park, K.-S.; Min, K.-M.; Seo, S.-D.; Lee, G.-H.; Shim, H.-W.; Kim, D.-W. Self-Supported Multi-Walled Carbon Nanotube-Embedded Silicon Nanoparticle Films For Anodes of Li-Ion Batteries. *Mater. Res. Bull.* **2013**, *48*, 1732−1736.
(22) Hieu, N. T.; Suk, J.; Kim, D. W.; Chung, O. H.; Park, J. S.; Kang, Y. Silicon Nanoparticle and Carbon Nanotube Loaded Carbon Nanofibers for Use in Lithium-Ion Battery Anodes. *Synth. Met.* **2014**, *198*, 36−40.
(23) Yu, W.-J.; Liu, C.; Hou, P.-X.; Zhang, L.; Shan, X.-Y.; Li, F.; et al. Lithiation of Silicon Nanoparticles Confined in Carbon Nanotubes. *ACS Nano* **2015**, *9*, 5063−5071.
(24) Wang, J.; Hou, X.; Zhang, M.; Li, Y.; Wu, Y.; Liu, X.; et al. 3-Aminopropyltriethoxysilane-Assisted Si@SiO2/CNTs Hybrid Microspheres as Superior Anode Materials for Li-ion Batteries. *Silicon* **2017**, *9*, 97−104.
(25) Gao, P.; Nuli, Y.; He, Y.-S.; Wang, J.; Minett, A. I.; Yang, J.; et al. Direct Scattered Growth of MWNT on Si For High Performance Anode Material in Li-Ion Batteries. *Chem. Commun.* **2010**, *46*, 9149−9151.
(26) Gao, P.; Jia, H.; Yang, J.; Nuli, Y.; Wang, J.; Chen, J. Three-Dimensional Porous Silicon-MWNT Heterostructure with Superior Lithium Storage Performance. *Phys. Chem. Chem. Phys.* **2011**, *13*, 20108−20111.
(27) David, L.; Asok, D.; Singh, G. Synthesis and Extreme Rate Capability of Si−Al−C−N Functionalized Carbon Nanotube Spray-on Coatings as Li-Ion Battery Electrode. *ACS Appl. Mater. Interfaces* **2014**, *6*, 16056−16064.
(28) Miroshnikov, Y.; Grinbom, G.; Gershinsky, G.; Nessim, G. D.; Zitoun, D. Do We Need Covalent Bonding of Si Nanoparticles on Graphene Oxide for Li-Ion Batteries? *Faraday Discuss.* **2014**, *173*, 391−402.
(29) Nessim, G. D.; Hart, A. J.; Kim, J. S.; Acquaviva, D.; Oh, J.; Morgan, C. D.; et al. Tuning of Vertically-Aligned Carbon Nanotube Diameter and Areal Density through Catalyst Pre-Treatment. *Nano Lett.* **2008**, *8*, 3587−3593.
(30) Teblum, E.; Itzhak, A.; Shawat-Avraham, E.; Muallem, M.; Yemini, R.; Nessim, G. D. Differential Preheating of Hydrocarbon Decomposition and Water Vapor Formation Shows That Single Ring Aromatic Hydrocarbons Enhance Vertically Aligned Carbon Nanotubes Growth. *Carbon* **2016**, *109*, 727−736.
(31) Nessim, G. D.; Al-Obeidi, A.; Grisaru, H.; Polsen, E. S.; Oliver, C. R.; Zimrin, T.; et al. Synthesis of Tall Carpets of Vertically Aligned Carbon Nanotubes by In Situ Generation of Water Vapor Through Preheating of Added Oxygen. *Carbon* **2012**, *50*, 4002−4009.
(32) Hata, K.; Futaba, D. N.; Mizuno, K.; Namai, T.; Yumura, M.; Iijima, S. Water-Assisted Highly Efficient Synthesis of Impurity-Free Single-Walled Carbon Nanotubes. *Science* **2004**, *306*, 1362−1364.
(33) Nessim, G. D.; Seita, M.; O'Brien, K. P.; Hart, A. J.; Bonaparte, R. K.; Mitchell, R. R.; et al. Low Temperature Synthesis of Vertically Aligned Carbon Nanotubes with Electrical Contact to Metallic Substrates Enabled by Thermal Decomposition of the Carbon Feedstock. *Nano Lett.* **2009**, *9*, 3398−3405.
(34) Grinbom, G.; Duveau, D.; Gershinsky, G.; Monconduit, L.; Zitoun, D. Silicon/Hollow γ-Fe2O3 Nanoparticles as Efficient Anodes for Li-Ion Batteries. *Chem. Mater.* **2015**, *27*, 2703−2710.

DOI: 10.1021/acs.jpcc.7b05709
J. Phys. Chem. C 2017, 121, 25632−25640

(35) Teblum, E.; Gofer, Y.; Pint, C. L.; Nessim, G. D. Role of Catalyst Oxidation State in the Growth of Vertically Aligned Carbon Nanotubes. *J. Phys. Chem. C* **2012**, *116*, 24522−24528.
(36) DiLeo, R. A.; Landi, B. J.; Raffaelle, R. P. Purity Assessment of Multiwalled Carbon Nanotubes by Raman Spectroscopy. *J. Appl. Phys.* **2007**, *101*, 064307.
(37) Osswald, S.; Havel, M.; Gogotsi, Y. Monitoring Oxidation of Multiwalled Carbon Nanotubes by Raman Spectroscopy. *J. Raman Spectrosc.* **2007**, *38*, 728−736.
(38) Obrovac, M. N.; Krause, L. J. Reversible Cycling of Crystalline Silicon Powder. *J. Electrochem. Soc.* **2007**, *154*, A103−A108.

DOI: 10.1021/acs.jpcc.7b05709
J. Phys. Chem. C 2017, 121, 25632−25640